The Effects of Different Mesh Generation Methods on Computational Fluid Dynamic Analysis and Power Loss Assessment in Total Cavopulmonary Connection

Yutong Liu

Kerem Pekkan

S. Casey Jones

Ajit P. Yoganathan
e-mail: ajit.yoganathan@bme.gatech.edu

Wallace H. Coulter Department of Biomedical Engineering,
Georgia Institute of Technology and Emory University, Atlanta, GA

The flow field and energetic efficiency of total cavopulmonary connection (TCPC) models have been studied by both in vitro experiment and computational fluid dynamics (CFD). All the previous CFD studies have employed the structured mesh generation method to create the TCPC simulation model. In this study, a realistic TCPC model with complete anatomical features was numerically simulated using both structured and unstructured mesh generation methods. The flow fields and energy losses were compared in these two meshes. Two different energy loss calculation methods, the control volume and viscous dissipation methods, were investigated. The energy losses were also compared to the in vitro experimental results. The results demonstrated that: (1) the flow fields in the structured model were qualitatively similar to the unstructured model; (2) more vortices were present in the structured model than in the unstructured model; (3) both models had the least energy loss when flow was equally distributed to the left and right pulmonary arteries, while high losses occurred for extreme pulmonary arterial flow splits; (4) the energy loss results calculated using the same method were significantly different for different meshes; and (5) the energy loss results calculated using different methods were significantly different for the same mesh. [DOI: 10.1115/1.1800553]

1 Introduction

In the normal heart, deoxygenated blood passes through the vena cava into the right ventricle, where it is pumped into the lungs through the pulmonary arteries to receive oxygen. The oxygenated blood then returns to the left heart, and the left ventricle pumps the blood into the body through the aorta. The single ventricle is a congenital heart defect in which the right side of the heart is hypoplastic or totally absent. This anomaly causes oxygenated and deoxygenated blood to mix in the single ventricle, thus reducing the amount of oxygen transferred to the body.

The total cavopulmonary connection (TCPC) is a surgical procedure introduced by de Leval et al. in 1988 [1] for the palliative repair of single-ventricle congenital heart defects. In this procedure (Fig. 1), the main pulmonary is disconnected from its ventricular origin, and the superior vena cava (SVC) is connected to the superior aspect of the right pulmonary artery (RPA). Finally, the inferior vena cava (IVC) is connected to the RPA by constructing a lateral tunnel through the right atrium or an external conduit that diverts blood around the right atrium [1–3]. As a result, the TCPC completely bypasses the right-hand side of the heart, and the single ventricle must drive blood throughout both the pulmonary and systemic circulations. Thus, a major issue for this procedure is the increased workload placed on the single ventricle. Previous investigations [4] have shown the energetic efficiency of the connection is critical for long-term success following TCPC operations.

The flow fields and energy losses in TCPCs with different geometric configurations and boundary conditions have been investigated by *in vitro* experiments [5,6] and computational fluid dynamic (CFD) studies. The previous CFD studies mainly focused on the effects of TCPC geometry and blood flow conditions on the fluid dynamics and energy efficiency of the TCPC. The TCPC geometry configurations that have been investigated include the diameters of the vena cava and pulmonary artery [7], the caval anastomosis offset [7–9], the anastomotic angle of the IVC and SVC [9,10], the size and shape of the IVC anastomosis [8], and the curved shape of the pulmonary artery [7,11]. The flow conditions studied in TCPC models include flow distribution between LPA and RPA [7], SVC-IVC flow-rate ratio [9], pulsation of the blood flow, SVC and IVC velocity profiles, and pulmonary artery pressure levels [12].

In addition to the energy losses in the TCPC [7,8,12], many flow parameters have been investigated including flow separation and recirculation [7–10], shear stress, and secondary flow patterns [9]. Different methods to calculate energy losses within the TCPC have also been studied. A technique that employs the viscous dissipation function as a tool for velocity gradient based estimation of fluid dynamic energy losses has been compared to the conventional control volume method [7,13]. Although the results from these preliminary studies were based on simplified TCPC geometries and flow conditions, they indicated that the design of the TCPC plays an important role in the fluid patterns and energetic efficiency of the anastomotic region.

Grid generation is an important and time consuming part of CFD analysis. The quality of the grid plays a direct role in the quality of the CFD analysis regardless of the flow solver used. Moreover, the flow solver will be more robust and efficient when using a well-constructed mesh. Structured grid generation methods take their name from the fact that the grid is laid out in a regular, repeating pattern called a block. These types of grids uti-

Contributed by the Bioengineering Division for publication in the JOURNAL OF BIOMECHANICAL ENGINEERING. Manuscript received by the Bioengineering Division January 30, 2004; revision received April 15, 2004. Associate Editor: J. Moore.

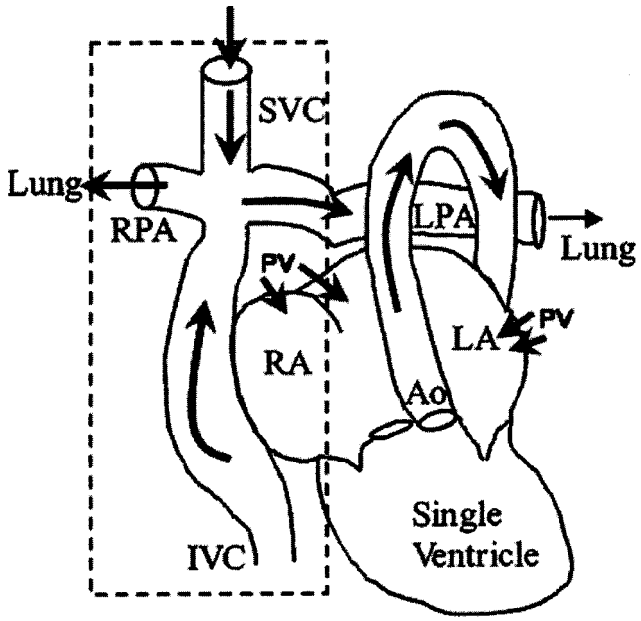

Fig. 1 Schematic shows the reconstructed circulation after an extra-cardiac total cavopulmonary connection surgery. The dashed box highlights the region of interest. LPA denotes the left pulmonary artery. PV denotes the flow of oxygenated blood in to the right and left atrium through the pulmonary veins.

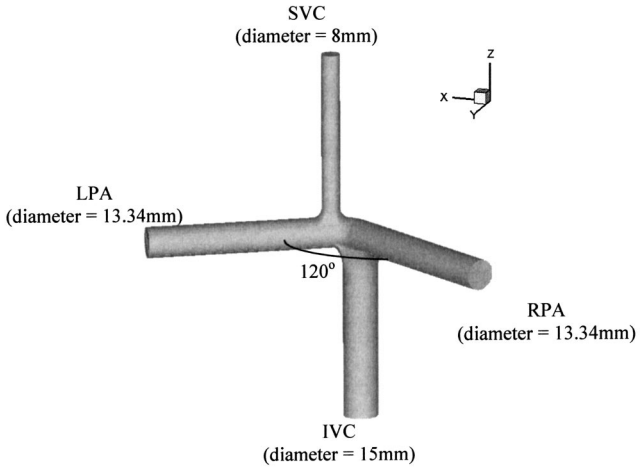

Fig. 2 TCPC model with physiological IVC diameter, SVC diameter, and curved PA

lize quadrilateral cells in 2D, and hexahedral cells in 3D, arranged in a rectangular array in computational space. Although the grid topology is fixed, the grid can be fitted to the body by stretching and twisting the blocks [14,15]. Structured grids have a considerable advantage over other grid topologies in that they give the user a high degree of control. Moreover, hexahedral and quadrilateral cells, which are very efficient at filling a space, can be highly skewed and stretched before the solution is significantly affected. This allows the user to cluster grid cells in regions of the flow field with high gradients and to use relatively fewer cells in areas with small gradients. Because the user interactively lays out the elements, the grid can be aligned with the flow to yield a more accurate solution. Structured flow solvers typically require the lowest amount of memory for a given mesh size and execute in less time because they can be optimized for the logical structure of structured grids. A final but important advantage of structured grids is that the post processing of the results is a relatively easy task because the logical arrangement of the grid coordinates makes it straightforward to plot the results. The major disadvantage of the structured grid is the time and expertise required to construct an optimal grid for an entire model. Complex 3D models can require even the most experienced user days or weeks to generate a suitable grid.

Unstructured grid generation methods utilize an arbitrary collection of cells to fill the domain. The mesh is called unstructured because the arrangement of cells has no discernible pattern. Unstructured grids typically utilize triangles in 2D and tetrahedrons in 3D. As with structured grids, the cells can be stretched and twisted to fit the domain. Unstructured grid generation methods are easily automated. A good mesh generation program can automatically place triangles on the surfaces and tetrahedrons in the volume of interest [16,17]. The advantage of unstructured grid methods is that they are automated and; therefore, require little user time or effort. As a result, unstructured grid generation methods are well suited for inexperienced users because they require little user input and will generate a valid mesh under most circumstances. Unstructured methods also enable the solution of large and detailed problems in minutes or hours instead of days or weeks like structured grid generation methods. The major drawback of unstructured grids is the lack of user control when laying out the mesh. Typically the user specifies information about the boundaries of the mesh, and the mesh generation program automatically fills the interior. Triangular and tetrahedral cells cannot be easily stretched or twisted; therefore, the grid must be largely isotropic, i.e., all the cells have roughly the same size and shape. This inflexibility is a problem when trying to resolve the flow in small areas with locally high velocity gradients, and often the entire grid must be made finer than necessary to resolve the flow in small but important areas of the domain. Unstructured flow solvers typically require more memory and have longer execution times than structured grid flow solvers on a similar mesh. Postprocessing of the solution on an unstructured mesh also requires powerful tools for interpolating the results onto planes and surfaces for visualization.

Given the above review, both methods of grid generation have desirable characteristics for the TCPC geometry. However, considering that the ultimate goal in using CFD to simulate the TCPC is to provide a surgical tool for the rapid modeling of patient-specific TCPC geometries in a clinical setting, the unstructured mesh generation method seems be to more suitable for the study of TCPC. Anatomically realistic TCPC models are unique and complex 3D geometries, and, in a clinical setting, the user generating the grid and flow solution will likely have neither the expertise nor the time to generate a high-quality structured grid. However, all of the previous CFD studies mentioned in the literature review above have used structured grids. Unstructured generation methods have not been used to study the TCPC. There has been no validation of unstructured grid methods and no comparison between structured and unstructured grid methods for CFD studies of the TCPC. The objective of this study is to verify the unstructured model with the structured model. To accomplish this objective, the flow field and energy loss results in these two models were compared. The models were generated based on an anatomically realistic TCPC geometry. The flow fields and energy losses were calculated at different flow split conditions. Different energy loss calculation methods [6,7] were also further studied with this TCPC model.

2 Numerical Methods

The computational simulations for this study were performed using CFD-ACE (Version 2002, CFD Corporation, Huntsville, AL). This package has been used previously by other investigators in TCPC studies [7,9]. CFD-ACE provides both structured and unstructured grid generation programs and flow solvers.

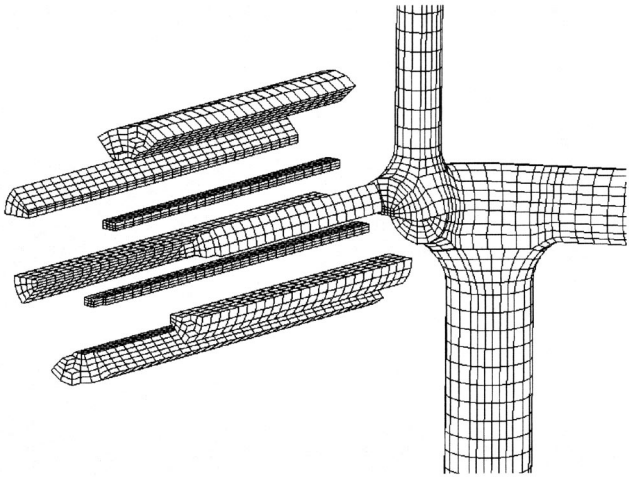

Fig. 3 Structured mesh for the TCPC model. Only the connection region and LPA are shown. The grid blocks of the LPA are decomposed and some cells are removed for better visualization.

2.1 Geometry of the TCPC model. Figure 2 shows the geometry of the TCPC model used in this study. The model has a physiological IVC diameter, SVC diameter, and curved pulmonary artery. The inner diameter of the pulmonary arteries is 13.34 mm. The inner diameters of the SVC and IVC are 8 mm and 15 mm, respectively, which were based on MRI data from an eight-year-old patient which Sharma et al. [5] and Ensley et al. [6] referenced to construct their models. The angle between the RPA and left pulmonary artery (LPA) at the connection is 120 deg based on the same MRI data. The site of caval anastomosis is offset by one diameter from the pulmonary artery. The geometries of the anastomoses of the SVC and IVC with the RPA are modeled as 4 mm and 7.5 mm constant-radius fillets, respectively. This geometry was chosen because it includes almost all the anatomic features of current interest. More important, it is neither too complex—facilitating relatively easier structured mesh generation, nor too simple—enabling a realistic comparison of the results from unstructured and structured models. The surface geometry was drawn using CFD-GEOM (the geometric modeling and mesh generation component of CFD-ACE), which supports a full range of 3D geometries including points, lines, arcs, circles, point interpolating curves and splines, and surfaces [18].

2.2 Mesh Generation. CFD-GEOM was also used to create the structured grid of the TCPC. The structured grid was generated using transfinite interpolation (TFI). CFD-GEOM supports uniform, exponential, geometric, and hyperbolic tangent grid point distributions along edges. Grid generation on curves was done directly on the curves themselves. Grid generation on surfaces was completed by projecting an approximate TFI grid directly onto the mathematical representation of the surface, or by computing the TFI grid in the parametric space of the surface. CFD-GEOM follows a bottom-up approach in labeling geometry elements as edges, faces, and blocks. The lines and curves that define the geometry were used to create edges, 4 logical edges to create a surface, and 6 logical surfaces to create a block [18]. The number of nodes on the edges determines the total number of hexahedral cells for each model. Cells were clustered near the anastomotic site since more complicated flow patterns were expected in the connection where the two inflows collide. Relatively fewer cells were placed at the inlets and outlets where the flow is relatively simple. A typical structured mesh of the TCPC model is shown in Fig. 3. The grid blocks of the LPA were decomposed to view the block arrangement and some cells in these blocks were removed to view the cell interface. The final structured mesh used in this study is composed of 26 blocks for a total of 917 240 hexahedral cells. The smallest cell volume is 2.31×10^{-3} mm^3, while the largest one is 0.303 mm^3. The smallest face angle is 1.11 (cf. Table 1). The parameters describing grid quality including skewness and aspect ratio were checked using CFD-GEOM and were well within the good quality range.

Table 1 Grid parameters for the structured mesh of the TCPC model

	N_{cell}[a]	$V_{\text{C max}}$ (mm^3)[b]	$V_{\text{C min}}$ (mm^3)[c]	$\alpha_{\text{f min}}$ (Deg)[d]
Mesh 1	117 951	2.150	2.69×10^{-2}	8.40
Mesh 2	354 494	0.580	9.22×10^{-3}	3.40
Mesh 3	917 240	0.300	2.31×10^{-3}	1.11

[a] N_{Cell} : number of cells.
[b] $V_{\text{C max}}$: largest cell volume.
[c] $V_{\text{C min}}$: smallest cell volume.
[d] $\alpha_{\text{f min}}$: smallest face angle.

Because unstructured grids are composed of different entities, different topological requirements exist for unstructured grid generation than for structured grid generation. Unstructured grids were created within unstructured domains. An unstructured domain is a user-defined solid region defined using surfaces that are grouped into surface sets. In 3D, the unstructured domain consists of one or more closed surface sets. A surface set consists of a set of connected loops or faces. The loop identifies the active portion of a surface to grid. Surface sets must be closed, and all entities within the set must be connected. A triangular grid is first generated on the surface set, and the user can control the minimum and maximum triangular cell size. The tetrahedral grid is generated in the interior of the volume automatically using the surface grid as a starting point [18]. A typical unstructured mesh of the TCPC model is shown in Fig. 4. In the figure, several cells were removed from the LPA to highlight the cell geometry and interfaces in the interior of the domain. The final unstructured mesh used in this study contains 602 378 tetrahedral cells. The smallest cell volume is 3.96×10^{-3} mm^3, and the largest cell is 0.258 mm^3. The smallest face angle is 13.9 (cf. Table 2). Like the structured mesh, the grid quality was adequate according to basic metrics calculated within CFD-GEOM.

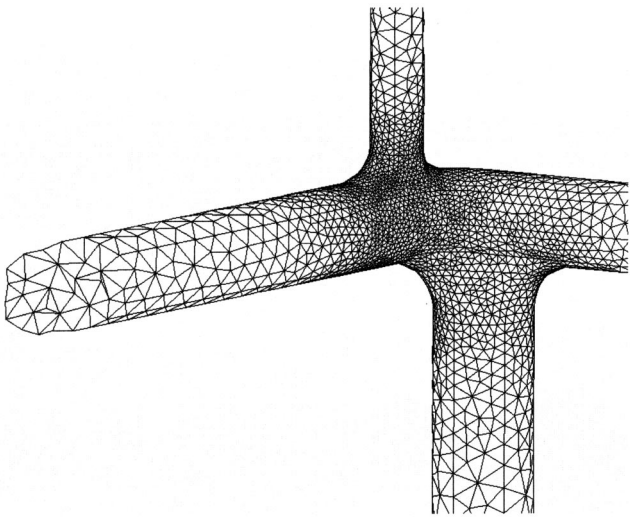

Fig. 4 Unstructured mesh for the TCPC model. Only the connection region and LPA are shown. Some cells in the LPA are removed for better visualization.

Table 2 Grid parameters of the unstructured mesh of the TCPC model

	N_{cell}[a]	$V_{C\,max}$ (mm^3)[b]	$V_{C\,min}$ (mm^3)[c]	$\alpha_{f\,min}$ (Deg)[d]
Mesh 1	60 917	15.70	1.89×10^{-4}	0.31
Mesh 2	122 356	1.330	9.53×10^{-3}	31.3
Mesh 3	334 853	0.455	3.42×10^{-3}	23.6
Mesh 4	602 378	0.258	3.96×10^{-3}	13.9

[a]N_{Cell}: number of cells.
[b]$V_{C\,max}$: largest cell volume.
[c]$V_{C\,min}$: smallest cell volume.
[d]$\alpha_{f\,min}$: smallest face angle.

2.3 Computational simulations. CFD-GUI, the general purpose fluid dynamics solver in the CFD-ACE package, was used to solve the computational model. First-order upwind differencing was used for the discretization of the convective terms. All computations for this study were performed on a Sun Ultra 80 workstation. The total cardiac output was assumed to be 4 liters/min. It was assumed that 40% of the total cardiac output entered the TCPC through the SVC with the remaining 60% entering through the IVC. The LPA and RPA pressures were varied so that LPA to RPA flow splits of 30:70, 40:60, 50:50, 60:40, and 70:30 could be obtained. The pressure values needed at the PA outlets for the desired flow splits were determined using trial-and-error. Figure 5 shows the linear trend line that was used for the structured model. A similar trend line was generated for the unstructured model. Other assumptions in the computational simulation and boundary conditions [7,13] were:

1. Blood was assumed incompressible and Newtonian (density $\rho = 1060\ kg \cdot m^{-3}$, viscosity $\mu = 3.5 \times 10^{-3}\ kg \cdot m^{-1} \cdot s^{-1}$;
2. Blood flow was assumed steady and laminar;
3. Vessel walls were assumed to be rigid and impermeable;
4. No-slip boundary condition was applied at the wall;
5. Inlet velocities were assumed to be uniform;
6. Outlet pressures were assumed constant across the vessels;
7. Outlet velocity profiles were computed assuming zero streamwise diffusion at the boundary.

Based on these assumptions, the maximum Reynolds numbers were 1030, 1290, and 1350 in the IVC, SVC, and PA, respectively.

2.4 Energy loss calculations. Energy losses were calculated using two methods: a control volume approach and a technique based on the energy dissipation function. Equation (1) shows the control volume analysis for energy loss computation:

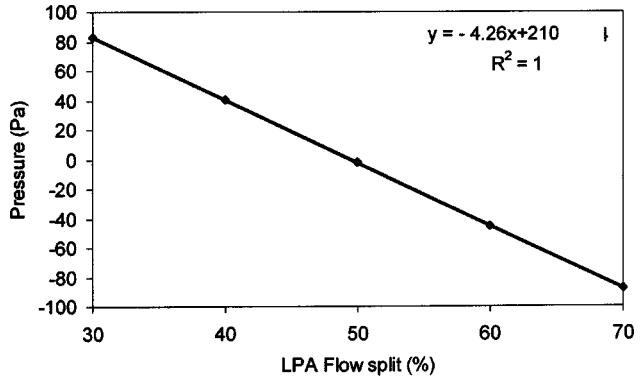

Fig. 5 Correlation plot used to determine outlet pressure boundary conditions in the structured models

$$\dot{E}_{loss} = -\int_{CS}\left[p_{static} + \frac{1}{2}\rho u_j u_j\right] u_i n_i dS \tag{1}$$

where CS is the control surface, p_{static} is the static pressure, u_i defines the components of the velocity vector, n_i represents the components of the outward surface normal vector of the control surface, dS is the area of the differential control surface, and $\dot{E}_{loss}$ is the rate of energy consumption within the control volume. This method is accurate but not immediately applicable in the clinical setting due to the method's reliance on pressure measurements across the whole inflow and outflow cross sections.

The CFD results were compared to the *in vitro* experiments. However, *in vitro* experiments provide only limited information about the pressure and velocity of the flow at the inlet and outlets of the TCPC domain. So a simplified version of Eq. (1), which is currently being used in *in vitro* experiments, was introduced to calculate energy loss with this limited information [6,7]:

$$\dot{E}_{loss} = -\sum\left(p_{static} + \frac{1}{2}\rho u_j u_j\right) u_i n_i A_i$$

$$= \sum P_{total} Q_{inlet} - \sum P_{total} Q_{outlet} \tag{2}$$

based on the following assumptions:

$$P_{total} \cong P_{static} + \tfrac{1}{2}\rho \overline{u_i}\,\overline{u_i}, \qquad \overline{u_i} = \frac{Q_i}{A_i}, \tag{3}$$

where Q_i represents the flow rate at an inlet or an outlet. Thus, Eq. (2) reduces the information needed for the energy calculation to the total pressure values and flow rates at the inlets and outlets.

The dissipation function method is based on the fact that, for laminar flow within rigid models, all the energy loss is due to friction. Such losses can be determined from the energy dissipation function, Eq. (4) [19,20]. The energy dissipation function represents the local fluid power losses produced by viscous dissipation. The integral of this value over the model volume is the energy loss of that model, Eq. (5) [7,13],

$$\phi = \frac{1}{2}\left(\frac{\partial u_i}{\partial x_j} + \frac{\partial u_j}{\partial x_i}\right)^2 \tag{4}$$

$$\dot{E}_{loss} = \mu \int_{CV} \phi \cdot dV \tag{5}$$

In these equations, ϕ is the dissipation function, CV represents the control volume over which power loss calculations are required, and dV represents the differential volume element within the control volume.

2.5 Grid sensitivity study. Grid size is always a limiting factor in any CFD study. A goal of this study was to compare different mesh generation methods; therefore performing grid sensitivity studies to guarantee mesh independent results was required. The energy losses calculated by the control volume and viscous dissipation methods were used as indices for the convergence of the solutions as the grids were refined. Three structured models and 4 unstructured models were generated to perform the grid sensitivity study. The mesh parameters for each model are shown in Tables 1 and 2. Figures 6 and 7 show the computed energy losses at the LPA 30%:RPA 70% flow split condition and CPU times as functions of the number of cells in the structured and unstructured models, respectively. All of the simulations were performed with the same assumptions, blood properties, and flow conditions. Apparently, the change of the energy loss increases with the number of cells logarithmically. In the structured model, the first mesh refinement from 117 951 to 354 494 cells produced the largest change in computed energy losses. The second mesh refinement did not show as large a change in the computed energy

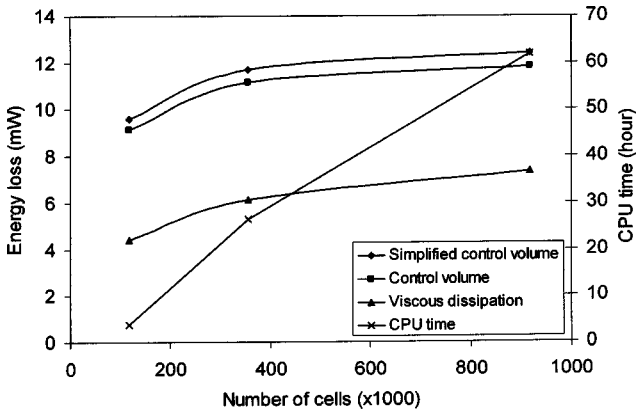

Fig. 6 Energy loss calculated with three methods (simplified control volume, control volume, and energy dissipation) and CPU time as a function of the number of cells in structured models

losses. The second refinement produced 5.8%, 5.5%, and 9.3% changes in energy losses with the simplified control volume, control volume, and viscous dissipation methods, respectively. In the unstructured model, the first two mesh refinements from 60 917 to 122 356 and to 334 853 produced the greatest change in energy losses; while mesh refinement beyond 334 853 cells only increased the energy loss by 3.6%, 5.2%, and 5.1% in simplified control volume, control volume and viscous dissipation methods, respectively. In both structured and unstructured models, the CPU time increased linearly with the number of cells in the mesh. Interestingly, however, the CPU time for the unstructured model was approximately the same as the structured model for a given number of cells, which is contrary to the expectation that structured models are computationally more efficient than unstructured models. However, it is suspected that much of the advantage of the structured grid was mitigated in this study by the multiblock topology of the structured grid, which was composed of 26 blocks. The overhead associated with this number of blocks is most likely responsible for the reduced computational efficiency of the structured solver. In this study, the finest meshes produced results that can be considered mesh independent for both structured and unstructured models. The finest meshes were used to compare the flow fields and energy losses predicted using the structured and unstructured models.

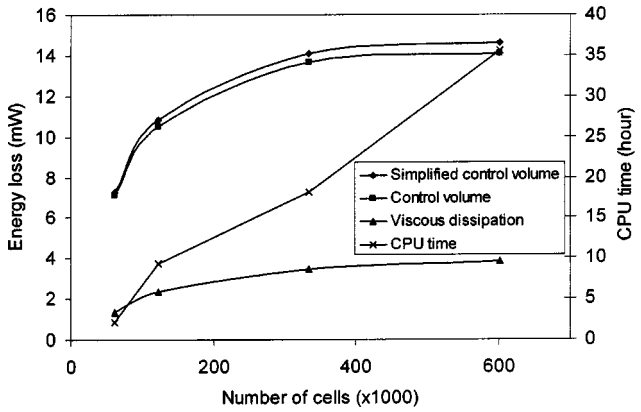

Fig. 7 Energy loss calculated with three methods (simplified control volume, control volume, and energy dissipation) and CPU time as a function of the number of cells in the unstructured models

3 Results

Streamtraces were plotted at the vertical and horizontal planes of the TCPC model as indicated in Figs. 8(*a*) and 8(*b*), respectively. These two planes were chosen because they include the connection region of the vena cava and pulmonary artery. It should be noted that these streamtraces are two-dimensional and confined to the plane. Due to the curved nature of this model in the vertical plane, only the pulmonary artery at the connection section can be seen, and, thus, the streamtraces in the pulmonary artery are slightly removed from the center plane. Figure 9 shows the streamtraces in the vertical plane of the structured (left panel) and unstructured (right panel) models with (*a*) 30%, (*b*) 50%, and (*c*) 70% of the total cardiac output directed towards the LPA. In the flow split condition of LPA 30%:RPA 70%, the fluid entering the connection region from the IVC flowed dominantly towards the RPA, while an almost equal amount of fluid from the SVC entered each PA. The SVC inflow impinged on the inferior aspect of the LPA just distal to IVC-to-LPA flare. A large area (16 mm in diameter) of flow having a clockwise rotation encompassed the entire central region of the connection between caval inlets. This central recirculation region appeared to be propelled by the IVC inflow on the RPA side and by the SVC inflow on the LPA side. The streamtraces in both models are similar, though the shape of the central recirculation is a little different. At equal outflows (LPA 50%:RPA 50%), the SVC inflow again impinged on the inferior aspect of the LPA, but a little further downstream from the LPA than in the LPA 30%:RPA 70% flow split. The recirculation region created by the SVC and the IVC inflows had a clockwise rotation with the size of about 11 mm. Again the shape of the recirculation is slightly different in the structured and unstructured models. At the LPA 70%:RPA 30% flow split, about equal

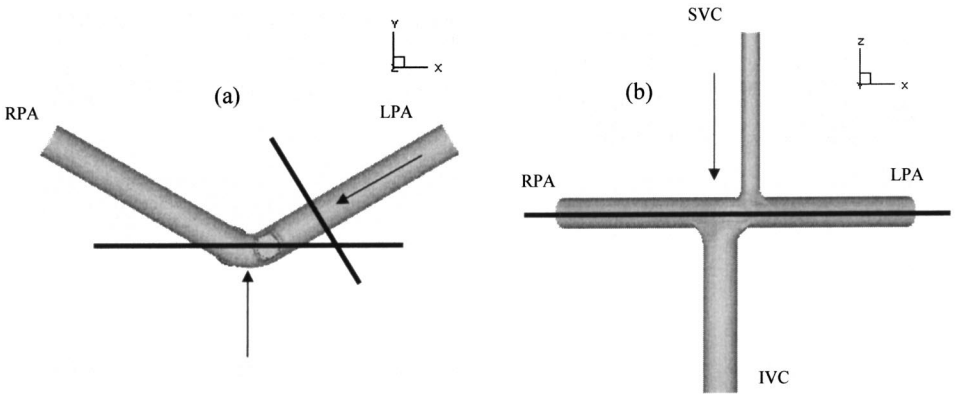

Fig. 8 Streamtraces on the (*a*) the vertical central plane and LPA cross section; and (*b*) the horizontal central plane. The arrows indicate the view direction.

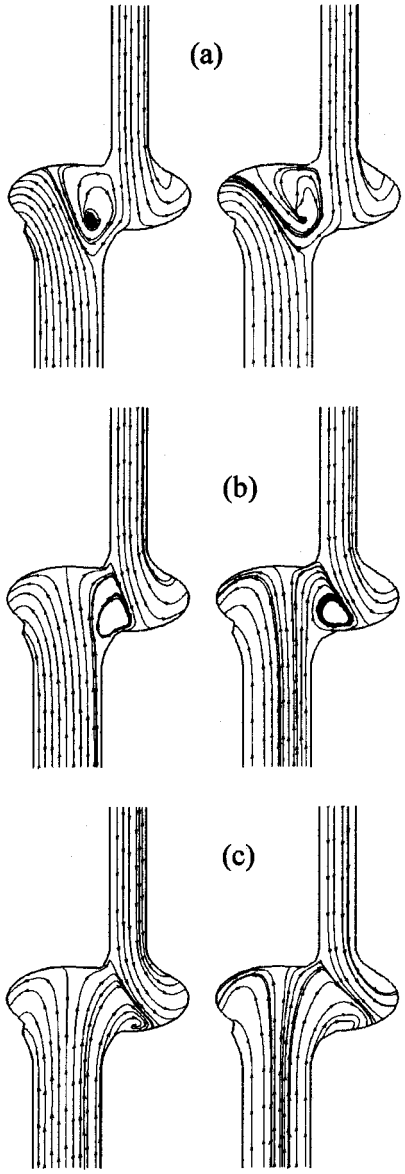

Fig. 9 Comparison of flow fields on the vertical plane in the structured (left panel) and unstructured (right panel) models at the flow split condition of (*a*) LPA 30%:RPA 70%; (*b*) LPA 50%:RPA 50%; (*c*) LPA 70%:RPA 30%

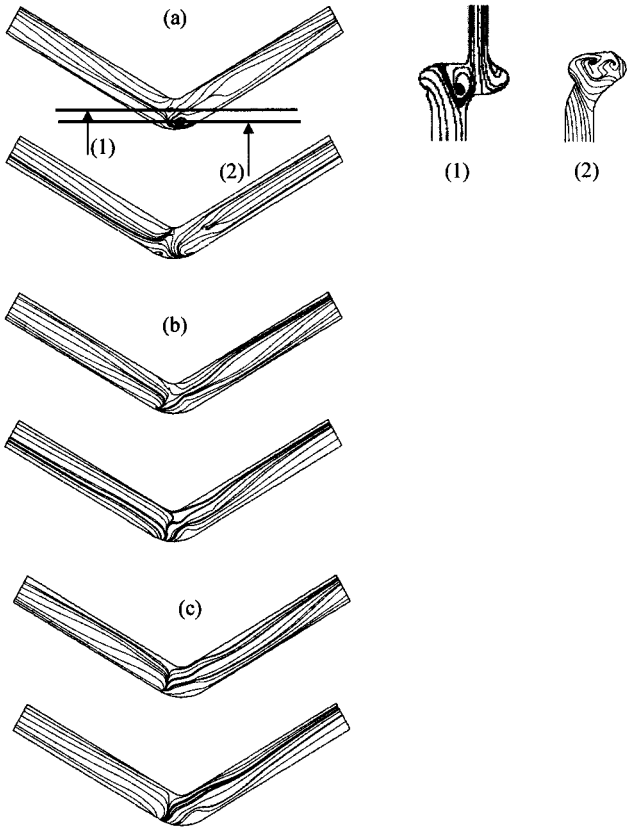

Fig. 10 Comparison of flow fields of the horizontal plane in structured (upper panel) and unstructured (lower panel) models at the flow split condition of: (*a*) LPA 30%:RPA 70%, in which (1) shows streamtraces in the vertical plane through the core of the small recirculation, and (2) through the core of the large recirculation (*b*) LPA 50%:RPA 50%; (*c*) LPA 70%:RPA 30%

amounts of the IVC inflow were directed towards each PA. The SVC inflow impinged on the inferior aspect of the LPA further downstream. A small recirculation zone (1 mm in diameter) occurred distal to the IVC-to-LPA flare, which is absent from the unstructured model.

The streamtrace plots of the horizontal plane are shown in Fig. 10. Figures 10(a)–10(c) show the streamtrace plots for the flow splits LPA 30%:RPA 70%, LPA 50%:RPA 50% and LPA 70%:RPA 30%, respectively. In each section of Fig. 10, the upper panel is the structured model while the lower panel is the unstructured model. For the flow splits of LPA 30%:RPA 70%, the IVC and SVC inflows in the structured model collided at the connection region and formed two vortices that are 1.5 mm and 5 mm in diameter, respectively. These two vortices were absent in the unstructured model. The streamtraces on the vertical planes through the cores of these two vortices were also plotted (see (1) and (2) in Fig. 10). It is apparent that these two vortices are three dimensional since they can be seen in both vertical and horizontal planes. It should be noted that the vertical plane through the small vortex is actually the central plane of the model, which is shown in Fig. 9. In the flow splits of LPA 50%:RPA 50% and LPA 70%:RPA 30%, no flow recirculation can be observed in either structured or unstructured models. The streamtraces become parallel at the LPA and RPA outlets.

Figure 11 shows the secondary flow on the cross section located two PA diameters distal to the SVC centerline [as shown in Fig. 8(a)]. At the flow split LPA 30%:RPA 70%, two counter-rotating vortices occurred in this cross section. These two vortices were approximately the same size. However, the size of the vortices in the structured model (~7 mm diameter) is larger than those in the unstructured model (~4 mm diameter). Increasing the flow in the LPA caused the vortex at the posterior side of LPA to become larger and the one on the anterior side to become smaller. This scenario occurred in both structured and unstructured models. However, again, the vortex in the structured model is larger than the corresponding one in the unstructured model. At a flow split of LPA 70%:RPA 30%, the anterior vortex had almost disappeared.

As described earlier, energy losses for each model were computed using three different methods: simplified control volume analysis, control volume analysis, and the velocity gradient based energy dissipation. Figure 12 shows the energy losses calculated by these methods in (*a*) the structured model and (*b*) the unstructured model. In both models, the calculation methods show the same trends with the LPA flow splits. Energy losses are highest at the extreme flow splits (LPA 30%:RPA 70% and LPA 70%:RPA 30%) and decrease to a minimum at the equal flow split. The largest energy loss difference among flow split conditions occurs

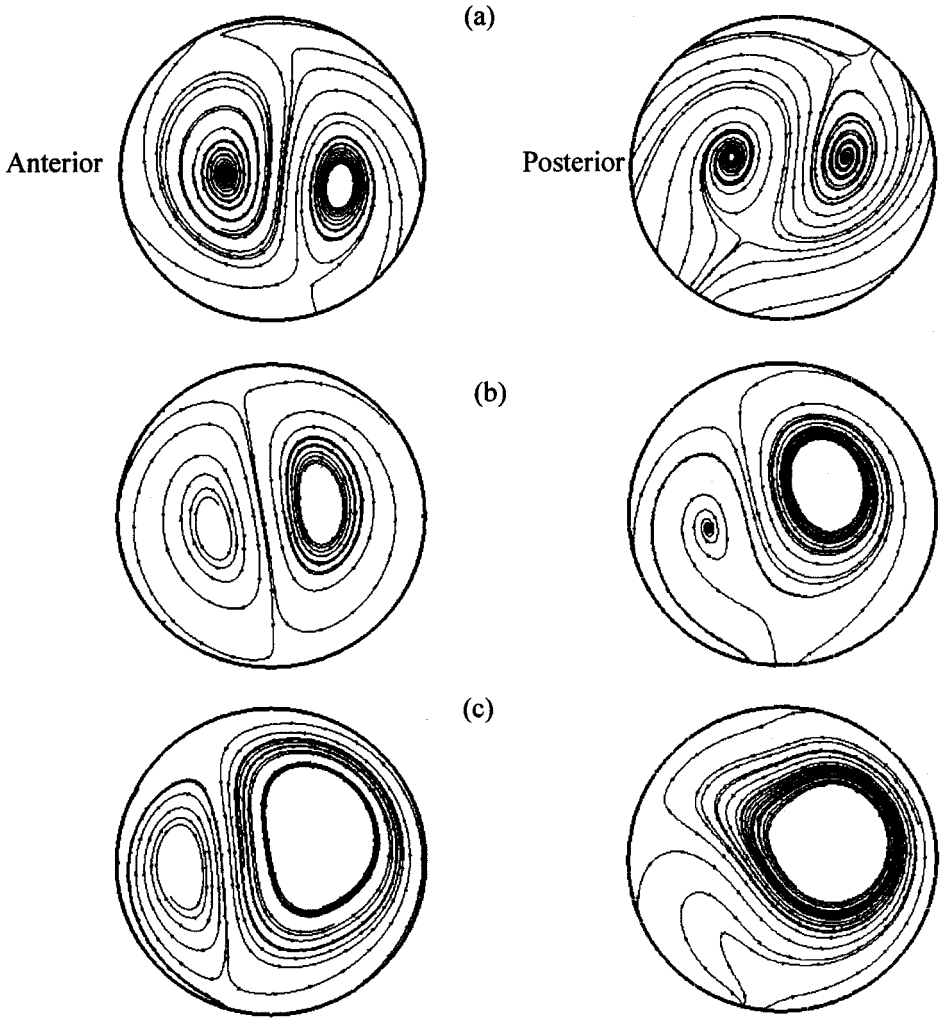

Fig. 11 Comparison of the secondary flow at the cross section two PA diameters from SVC centerline in structured (left panel) and unstructured (right panel) models at the flow split condition of (*a*) LPA 30%:RPA 70%; (*b*) LPA 50%:RPA 50%; (*c*) LPA 70%:RPA 30%

in the structured model calculated using the viscous dissipation method. The energy loss at LPA 30%:RPA 70% is 17.0% higher than that at the flow split LPA 50%:RPA 50%. The smallest difference is in unstructured model using the viscous dissipation method, where the energy loss at LPA 30%:RPA 70% is 4.00% higher than that at the equal flow split. The simplified control volume and control volume methods give energy losses that are closer to each other. The largest difference between these two methods is 5.00%, which occurs in the structured model at LPA 70%:RPA 30%. In the unstructured model, the largest difference is 3.60% at LPA 70%:RPA 30%. *In vitro* experimental results from our group are also included in Fig. 12. The simplified control volume method is the closest to the experimental results. The largest difference between these two sets of results is 44.3% in the structured model and 24.7% in unstructured model both at LPA 70%:RPA 30%. Figure 13(a) shows the energy losses calculated by the simplified control volume analysis in both structured and unstructured models as a function of LPA flow split compared to the experimental results. Clearly, the unstructured results are closer to the experimental results than the structured ones. The largest difference between the structured and unstructured models is 37.4% at LPA 60%:RPA 40%. The energy losses calculated using the control volume and viscous dissipation methods are also significantly different between these two models as shown in Figs. 13(*b*) and 13(*c*). The largest difference is 38.2% with the control volume method at LPA 60%:RPA 40% and 38.1% with viscous dissipation method at LPA 30%:RPA 70%.

4 Discussion

This study shows that the flow fields generated using structured and unstructured grids are qualitatively similar. The most significant difference occurred at the LPA 30%:RPA 70% flow split where the structured grid produced more vortices in the connection region. A strong secondary flow occurred in the pulmonary artery, and the size of the vortices in this secondary flow was larger in the structured model. Based on these results, the structured model appears to capture more vortices than the unstructured model. For all the vortices captured by both models, the shape was also slightly different using different mesh methods. These differences are likely caused by differences in the way the convective terms are calculated in the two grid topologies. That is, the structured and unstructured mesh solvers use different methods, for example, neighbor control-volume searching and interpolation from cell center to cell face. Particularly, any flux entering to the control volume is calculated from the neighbor cells through complex interpolation methods that govern the physics of fluid dynamics. In structured grids geometries of the neighbor

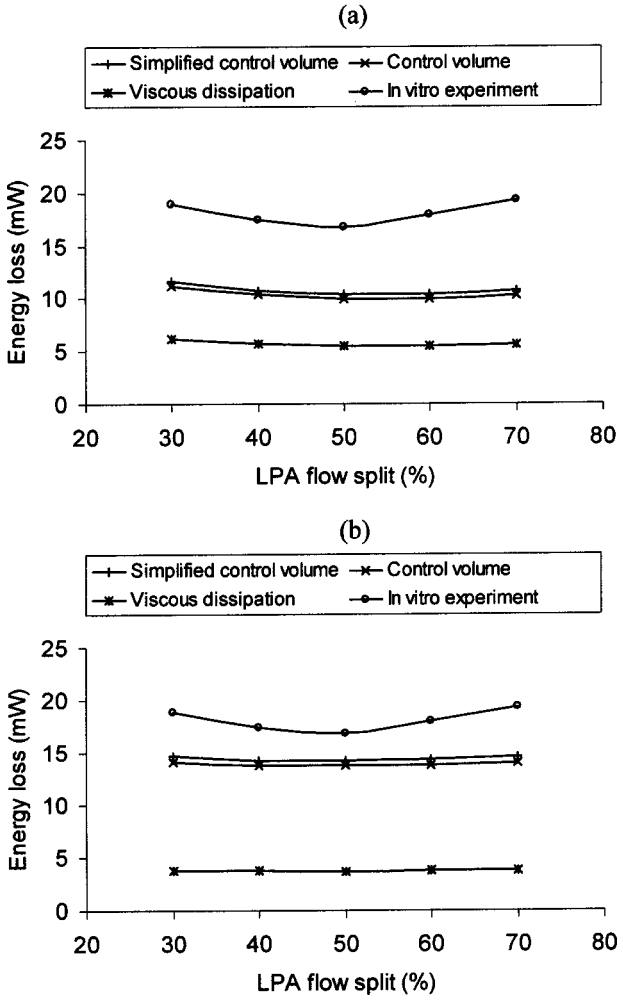

Fig. 12 Energy loss assessment by different calculation methods plotted against the different LPA flow split conditions in the (*a*) structured model and (*b*) unstructured model

cells, cell faces are well defined, while in unstructured grids this information is very irregular. For this reason in unstructured grids, flux terms needs to be calculated through more complex techniques. In many problems, especially having smooth, well defined flow direction (e.g., a boundary layer flow) or there are larger flow structures (e.g., a large vortex in a lid-driven flow), structured grids will produce better results than unstructured grids since the physical flux directions will be aligned with the cell faces. When the flow becomes complex and spatially irregular, in terms of cell-face-flux/flow directions, structured grids can also be considered irregular. For these cases, unstructured grids might do a better job since they will have an additional freedom in the cell face orientation relative to flow (in the flux calculation, if an error is made in one of the cell faces, it will probably be corrected in a neighboring cell having the correct cell face/flow orientation) while structured grids will not have such chance, as they have an arbitrary (in complex models independent from the local flow structure) directional bias. Moreover in the solver itself, flux interpolation algorithms of unstructured grids are inherently designed to handle the irregular cell face/flow orientations in all problems while structured solvers may use algorithms that are less general, as everything in the domain is assumed structured. It is reasonable that the differences in flow fields observed here are due to these and other similar intrinsic differences in the structured and unstructured flow solvers.

The energy loss results showed that the structured and unstructured mesh generation methods have significantly different energy loss calculations (higher than 30% in all three methods). The energy losses from the simplified and regular control volume methods were higher in the unstructured model; whereas, the viscous dissipation method yielded higher energy losses in the structured model. The second scenario can be explained by the fact that the structured model can capture more vortices than the unstructured model where most of the viscous dissipation occurs. The viscous dissipation analysis is based on the velocity gradient, which is very sensitive to the grid size and shape. The differences in the visually similar flow fields of structured and unstructured models are magnified by the velocity gradient calculation. It is hard to explain why the energy losses are higher in the unstructured model in the control volume methods. As mentioned by Ryu et al. [7], comparing the kinetic energy loss term to the pressure loss term in the control volume energy loss calculation, shows that most of the energy loss is caused by the pressure drop. The kinetic energy loss is relatively small. The pressure drives the blood through the TCPC model. The differences in the flow fields in these two models are certainly caused by different pressure drops. Both larger pressure drops and smoothened out small scale vortices of unstructured grids can also be attributed to the excessive numerical dissipation introduced to the solution by the solver. The complexity of discretization schemes used with unstructured grids is known to introduce a higher numerical dissipation into the CFD solution, compared to structured schemes. However, it is difficult to quantify and isolate this effect in complex models, unless further investigations are performed with controlled unstructured grid geometries.

Healy et al. [13] compared the energy losses calculated by the control volume and viscous dissipation methods in a planar constant vessel diameter TCPC model and found no significant difference in the energy losses (less than 6%) between the two methods. However, in this study, the energy losses from these two methods have huge differences. Ryu et al. [7] also found energy losses that were 35% different in these two methods in a planar TCPC model with anatomically accurate vessel diameters. They also found that as the geometry became more complicated, the CFD results drifted further away from the experimental results. The results presented here taken with Ryu et al. [7] suggests that Healy's [13] conclusion may not hold for complex TCPC models. It should be noted that only structured meshes were used in Ryu et al. [13]. Another possible explanation for differences in the energy losses calculated using the dissipation and control volume methods is that energy conservation is not guaranteed by the numerical simulation. (Note that mass and momentum conservation are guaranteed for a converged solution.) This might be another reason for the poor viscous dissipation results. In other words, the error might not be induced by the viscous dissipation method itself but by the numerical simulation, which does not guarantee the energy conservation.

Although it is not the objective of this study to compare the results from CFD and *in vitro* experiments, it is still interesting to see that the *in vitro* experiment yielded the same energy loss trend as the CFD, and the energy loss values were significantly different from the CFD. It is also worth mentioning that the CFD models used in this study assumed the flow to be steady. It has been reported recently [21] and confirmed by our preliminary experiments that the stagnation flow caused by two inflows is unstable and can cause the global flow to become unsteady. As the model complexity and Reynolds numbers increase, these unsteady effects are expected to become more and more important.

The grid sensitivity studies show the convergence of the results occurred at about 400 000 cells in both models. This cell number is much larger than previous studies where grids with 10 000–70 000 cells were used [7–9]. Since most of these studies had similar basic assumptions such as rigid walls, steady flow, Newtonian fluid, laminar flow, this huge difference in cell number might be due to the fact that the model used in this study is more

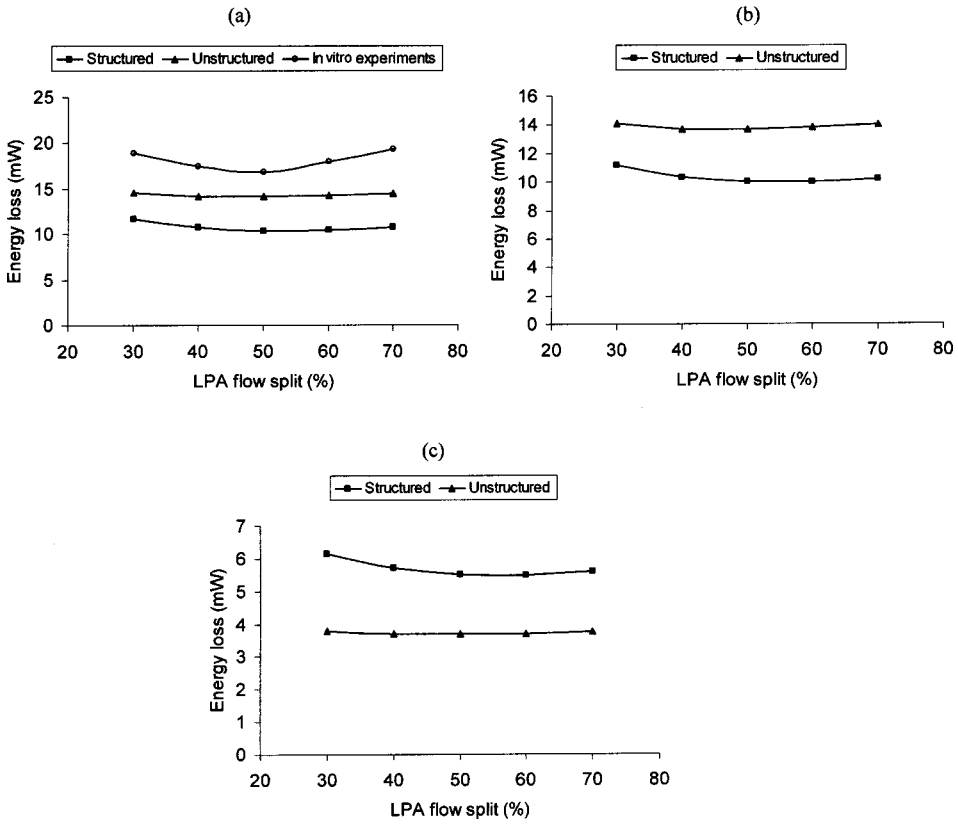

Fig. 13 Energy loss assessment in different models plotted against the different LPA flow split conditions by (*a*) simplified control volume method, (*b*) control volume method, and (*c*) velocity gradient based viscous dissipation analysis

anatomically realistic, and the model volume is relatively large compared to some previous studies. The convergence criterion is also an important factor. In this study, we used energy loss results as the criterion. Using other criteria such as the velocity profile or shear stress may require a different number of cells for grid independence. It is also interesting that in this study even though the energy loss results from different calculation methods are significantly different, the curves of the energy loss versus the mesh density for all the three methods have a similar shape.

Previous studies [6,7] have shown the promise of CFD combined with the viscous dissipation method as a noninvasive means (through the MRI velocity data) of determining TCPC energy losses in the clinical setting. By using this strategy, pediatric cardiologists and cardiac surgeons could simulate different TCPC surgical options and obtain an estimate of postoperative connection power losses. Thus, surgical planning protocols and methods could be validated prior to clinical implementation. The postoperative efficiency of TCPC surgeries could also be assessed by this strategy. In clinical practice, the TCPC geometry will be more complex than the model TCPC geometry used in this study. This complexity makes structured mesh generation very difficult, if not impossible, and makes the unstructured mesh attractive. This study tried to verify the unstructured mesh against the structured mesh and *in vitro* experiments. Although the results are not plausible, they demonstrate the potential of this strategy being used for comparisons in clinical practice, i.e., searching for the optimal strategy among several TCPC surgical plans. Based on the results presented here; however, it is unlikely that the absolute value of the energy loss can be accurately predicted given the current limitations of CFD methods and computational power.

5 Conclusion

This study showed that the flow fields in the structured and unstructured TCPC models are qualitatively similar under most LPA flow split conditions. Energy losses calculated in the structured and unstructured models are significantly different. However, the energy loss distribution among the LPA flow splits was the same for both models. The control volume methods on the unstructured mesh produced the most accurate energy losses as compared to the *in vitro* experiment.

Complex nontrivial relationships among factors such as numerical scheme, flow complexity, grid distribution, dissipation and boundary conditions influence CFD simulations. This study has value in that it took a real-world case and studied it at grid resolutions that are larger than normal but *practical* and found distinct differences in the predicted flows and energy losses. Especially, these differences were not as large for other less complex Fontans like those by Healy and Keesuk [7], which has the presented implications as the flows studied become more and more realistic and complex.

The feasibility of using the velocity gradient based dissipation method previously reported by Healy et al. [13] for assessing the energetic efficiency of the TCPC was also investigated. This study indicated that this method is not ready to be exclusively used for TCPC models with complex geometry. The large gap between the control volume and viscous dissipation methods needs to be further studied. Again however, these methods give the same trend for energy losses with changing LPA flow split. Therefore, such studies can be used in comparative projects after the error has been completely assessed. Higher order spatial discretization schemes, especially when combined with time accurate direct nu-

merical simulations, would improve the results of flow fields and energy losses. However, at the Reynolds number range considered here, these simulations will still have high computational costs and would not be practical in the clinical pace. For possible future improvement with the same TCPC model, studies with these alternate numerical methods and CFD solvers are in progress.

Acknowledgment

This study was supported by the National Institute of Health Grants Nos. NHLBI-5R01 and HL067622-02.

References

[1] de Leval, M. R., Kilner, P., Gewillig, M., and Bull, C., 1988, ''Total Cavopulmonary Connection: A Logical Alternative to Atriopulmonary Connection for Complex Fontan Operations. Experimental Studies and Early Clinical Experience,'' J. Thorac. Cardiovasc. Surg., **96**, pp. 682–695.

[2] Jonas, R. A., and Castaneda, A. R., 1988, ''Modified Fontan Procedure: Atrial Baffle and Systemic to Pulmonary Artery Anastomosis Technique,'' J. Card. Surg., **3**, pp. 91–96.

[3] Puga, F. I., Chiavarelli, M., and Hagler, D. J., 1987, ''Modifications of the Fontan Operation Applicable to Patients With the Left Atrioventricular Valve Atresia or Single Atrioventricular Valve,'' Circulation, **76**, pp. III-53–III-60.

[4] de Leval, M. R., 1998, ''The Fontan Circulation: What Have We Learned? What to Expect?'' Pediatr. Cardiol., **19**, pp. 316–320.

[5] Sharma, S., Goudy, S., Walker, P., Panchal, S., Ensley, A., Kanter, K., Tam, V., Fyfe, D., and Yoganathan, A., 1996, ''*In Vitro* Flow Experiments for Determination of Optimal Geometry of Total Cavopulmonary Connection for Surgical Repair of Children With Functional Single Ventricle,'' J. Am. Coll. Cardiol., **27**, pp. 1264–1269.

[6] Ensley, A. E., Lynch, P., Chatzimavroudis, G. P., Lucas, C., Sharma, S., and Yoganathan, A. P., 1999, ''Toward Designing the Optimal Total Cavopulmonary Connection: An *In Vitro* Study,'' Ann. Thorac. Surg., **68**, pp. 1384–1390.

[7] Ryu, K., Healy, T. M., Ensley, A. E., Sharma, S., Lucas, C., and Yoganathan, A. P., 2001, ''Importance of Accurate Geometry in the Study of the Total Cavopulmonary Connection: Computational Simulations and *In Vitro* Experiments,'' Ann. Biomed. Eng., **29**, pp. 844–853.

[8] Dubini, G., de Leval, M. R., Pietrabissa, R., Montevecchi, F. M., and Fumero, R., 1996, ''A Numerical Fluid Mechanical Study of Repaired Congenital Heart Defects: Application to the Total Cavopulmonary Connection,'' J. Biomech., **29**, pp. 111–121.

[9] Khunatorn, Y., , Khunatorn, Y., DeGroff, S. G., and Shandas, R., 2002, ''Influence of Connection Geometry and SVC-IVC Flow Rate Ratio on Flow Structures Within the Total Cavopulmonary Connection: A Numerical Study,'' J. Biomech. Eng., **124**, pp. 364–377.

[10] Migliavacca, F., de Leval, M. R., Dubini, G., Pietrabissa, R., and Fumero, R., 1999, ''Computational Fluid Dynamic Simulations of Cavopulmonary Connections With an Extracardiac Lateral Conduit,'' Med. Eng. Phys., **21**, pp. 187–193.

[11] Gerdes, A., Kunze, J., Pfister, G., and Sievers, H., 1999, ''Addition of a Small Curvature Reduces Power Losses Across Total Cavopulmonary Connections,'' Ann. Thorac. Surg., **67**, pp. 1760–1764.

[12] Migliavacca, F., Kilner, P. J., Pennati, G., Dubini, G., Pietrabissa, R., Fumero, R., and de Leval, M. R., 1999, ''Computational Fluid Dynamic and Magnetic Resonance Analyses of Flow Distribution Between the Lungs After Total Cavopulmonary Connection,'' IEEE Trans. Biomed. Eng., **46**, pp. 393–399.

[13] Healy, T., Lucas, C., and Yoganathan, A., 2001, ''Noninvasive Fluid Dynamic Power Loss Assessments for Total Cavopulmonary Connections Using the Viscous Dissipation Function: A Feasibility Study,'' J. Biomech. Eng., **123**, pp. 317–324.

[14] Thompson, J. F., and Weatherill, N. P., 1998, ''Fundamental Concepts and Approaches,'' in *Handbook of Grid Generation*, edited by Thompson, J. F., Soni, B. K., and Weatherill, N. P., CRC Press.

[15] Spekreijse, S. P., 1998, ''Elliptic Generation Systems,'' in *Handbook of Grid Generation*, edited by Thompson, J. F., Soni, B. K., and Weatherill, N. P., CRC Press.

[16] Weatherill, N. P., 1998, ''Introduction to Unstructured Grids,'' in *Handbook of Grid Generation*, edited by Thompson, J. F., Soni, B. K., and Weatherill, N. P., CRC Press.

[17] Baker, T. J., 1998, ''Delaunay-Voronoi Methods,'' in *Handbook of Grid Generation*, edited by Thompson, J. F., Soni, B. K., and Weatherill, N. P., CRC Press.

[18] CFD Research Corporation, 2002, CFD-GEOM User Manual, Version 2002, CFD Research Corporation, AL.

[19] Bird, R., Stewart, W., and Lightfoot, E., 1960, *Transport Phenomena*, John Wiley.

[20] Currie, I. G., 1993, *Fundamental Mechanics of Fluids*, McGraw–Hill.

[21] Khunatorn, Y., Shandas, R., DeGroff, C., and Mahalingam, S., 2003, ''Comparison of *In Vitro* Velocity Measurements in a Scaled Total Cavopulmonary Connection With Computational Predictions,'' Ann. Biomed. Eng., **31**, pp. 810–822.